Submitted for publication

A Multi-Scale Model of Intergranular Fracture and Computer Simulation of Fracture Toughness of a Carburized Steel

Su Hao[1]*, H. Lin[2], Robert R. Binomiemi[3], Dana M. G. Combs[4],, Greg Fett[4]

[1]Department of Mech. Engineering,
Northwestern University, Evanston, IL 60208
E-mail: suhao@northwestern.edu, hao0@suhao-acii.com
[2]Materials and Processes Eng. Dept. (MPED), GE Aviation, Cincinnati, OH 45215
E-mail: hong.lin@ge.com
[3]Heavy Vehicle Technology Group, Dana Corporation, Kalamazoo, MI 49009
E-mail: bob.binoniemi@dana.com
[4]Automotive Systems Group, Dana Corporation, 3939 Technology Drive, Maumee, OH 43537
E-mail: dana.combs@dana.com
E-mail: greg.fett@dana.com

Key words: Carburized Steel, Fracture Toughness, Multi-Scale, Intergranular Fracture, grain boundary

ABSTRACT

Breakthrough of computational alloy's design lies in the capabilities to quantitatively and completely integrate key-mechanisms in each processing step into a unified procedure that is able to establish the quantitative relationship between chemical composition, nano/microstructures, properties and performance. For this purpose, a multi-scale model of intergranular fracture has been developed to analysis the directly quenched after carburizing, carburized steels. This class of steels is highly susceptible to intergranular fracture which often results in relatively low fracture toughness. To achieve improved performance, the crucial issues are to clarify the dominant mechanisms that cause fracture and to distinguish the effects of alloy additions and impurities on the transition between intergranular and transgranular failure modes. Based on the computations at micro and quantum scales, the developed procedure has been applied for the AISI 8822 with carburized case steel, providing the prediction of fracture toughness that is compared with experiments. This analysis reveals that an integranular cracking is mainly triggered by the triple-junction stress concentration when grain boundary adhesion is low. An improved toughness can be achieved by reducing impurities grain boundary segregation while increasing grains' ductility.

Keywords

grain boundary, interfacial adhesion, first-principle, carburized steel, intergranular fracture, fracture toughness, multi-scale model

---

[*] To whom correspondence should be addressed

1. INTRODUCTION

Although rapidly development of computational engineering science continuously provides new means and tools to investigate deformation, fracture and failure phenomena of alloys, challenge remains in obtaining quantitative relationships between chemical composition and alloy compounds, micro and nano structures, micro and macro properties, laboratory characterization and engineering performance through hierarchically integrating key-mechanisms at each process step while highlighting dominant mechanisms, so as to enable a thoroughgoing computational material's design.

Quantum mechanics provides fundamental knowledge of the atomic-electronic structures of a material, which determines corresponding micro and macro properties[1-4,11,12,26]. To investigate material's properties in general, at sub-atomic scale a metal is usually treated as a bulk phase formed by periodic atomic array that obeys Bloch's theorem [67]. However, a metal's failure is often triggered by structural discontinuities in lattice; for example, dislocations. At microscale the random-distributed heterogeneities such as grains, second phase particles, and solution atoms, essentially dominate the kinetics of an alloy when environment changes[5-9,19,20,23,24,43]. Nevertheless, at macro-scale a structural evolution, for example, a plastic deformation that is an average of lattice's distortion and dislocation, is often modeled again under the approximations of uniform and continuous through constitutive relationship like stress-strain law in the framework of continuum mechanics [10,13-18,43]. This bottom-up, hierarchical variations in material's structural modeling reflect the challenges remaining for alloys' design, which also reveal the natural complexity of a material. An effective and quantitative analysis procedure to integrate sub-atomic physics with up-atomic mechanisms will bring significant benefit for exploring new materials with lower cost and better performance. An effort has been made in this paper is to develop such a procedure to study the failure mechanisms at different scales that may affect the fracture toughness of carburized steels case.

Directly quenched after carburizing, carburized steels, are traditional materials for machine components like gears in heavy energy transmission systems [19,21,22]. The case microstructure of this class of steels consists of low temperature tempered martensite and retained austenite, which is highly susceptible to intergranular fracture that often results in relatively low fracture toughness. Fig. 1 is a fractography of an AISI 8822 fully carburized specimen with multiple intergranular cracks. To achieve improved performance, it is vital important to clarify the mechanisms that cause intergranular cracking and to distinguish the effects of alloy additions and impurities on the transition between intergranular and transgranular failure modes, so as to find optimized chemical composition and heat treatment process for desirable properties.

Based on the literatures cited in this paper and the authors' previous works [20, 25], a multi-scale analysis model of the intergranular fracture in carburized steels case is proposed and an associated computation-based procedure is developed. This approach focuses on grain and grain boundary properties, especially phosphorous segregation, and their effects on the steel's fracture toughness. This procedure hierarchically implements the quantum mechanical computation into a microscale polycrystalline system with plasticity finite elements and cohesive law, which is embedded into the computation of a laboratory-sized specimen to predict fracture toughness. As an example of application, the analysis of AISI 8822 carburized case steel is performed and the obtained results are compared with experiments. The main object of this paper is to introduce the concept, methodology, and main scheme of the developed procedure. The detailed algorithms at each scale are either described in the cited literatures or just briefly listed in the Appendices.

Reviews and analysis of the microstructures and failure mechanisms of carburized steels can be found, e.g. in [19,21-23]. Dislocation kinetics involved grain boundaries and interfacial properties have been introduced, e.g. by [23] in the perspective of physical metallurgy and by [15, 36] in solid mechanics. To link grain boundary properties with alloy's mechanical properties, an impurity segregation model has been developed in [6]. Thermodynamics analysis and more generalized investigations of grain boundaries chemistry can be found, e.g. in [7, 23]. Based on the "universal feature" [26] of atomic bonding [11,12,67], interfacial debonding and cohesive models for solid mechanical computations have been proposed in [15,29] with the applications for bulk phase fragmentation [38] and interfacial crack propagation [36]. A systematical study of the elastoplastic constitutive model for polycrystalline system has been introduced in [9]. Regarding the general issues of grains and grain boundaries, researches and developments have been reported, e.g. in [18, 34, 35, 55, 66] of crystal plasticity, in [31-33] of impurities grain boundary segragation, in [43] of grain boundary creep and sliding, in [6, 7, 31] of intergranular fracture, in [68,69] of the length scale in plasticity and in [39, 13, 14, 40-42] of fracture mechanics. Literatures of computation science in general can be found, e.g. in [44-49, 70, 71] of the density function theory [2,3] based quantum mechanics computation and in [50-53] of finite element.

In recent years great activities can be found regarding multiscale analysis and its application to materials science, for examples, these in [57-63, 20, 28]. In [63] a scheme has been proposed to compute the average heat conductivity of a cell containing aggregated heterogeneous composite inclusions through the cell's surface heat flow and temperature. This model has its counter part in solid mechanics analysis, i.e. the cell model originally developed in [64]. A quasicontinuum method, by which the basic unit is a finite element that contains atoms, has been developed in [60,61]; the energy potential of the "embedded atomic method (EAM)" [48,49] has been adopted as the strain energy in the finite element. In the "coarse-grain" method [58] an atomic segregate forms finite element to represent a thermodynamic system, by which both mechanical deformation and statistic-based thermo-vibration-induced temperature are taken into account. A concurrent scheme between different physical domains in continuum theory has been developed in [62]. A formalism coupling density-function theory-based simulation in one domain to the continuum mechanics simulation in another domain has been developed in [57]. A "Moving Particle Finite Element Method" (MPFEM) has been developed in [20, 25, 27, 30], which combines the salient features of finite element and particles to represent a solid. In order to accurately and efficiently represent atomistic behavior at microscale, a "Particle Dynamics"(PD) method has been developed in [20,28]. The MPFEM and PD are the computational methods applied in this study; detailed description of the "Particle Dynamics" and application to bcc iron are given in the sections 2.5-2.7 of [20]. The original concept for this class of methodologies can be found in the Lorentz's original work that establishes the connection between mean field electrostatic theory and microscopic theory, as described by the chapter 27 of [67].

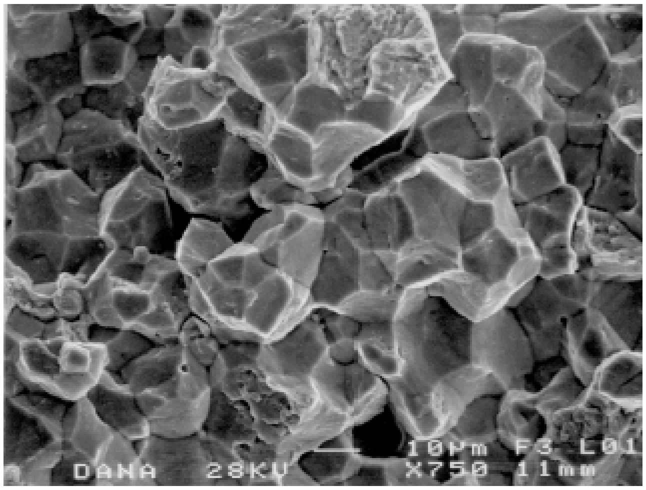

Fig. 1 An experimental observation of intergranular fracture

2. MODEL AND PROCEDURE DEVELOPED

2.1 An Integranular Fracture Model

For an engineering component such as a gear under cycling contacts, the hardeness, strength and fracture toughness at its carburized case are the governing properties that determine performance. High case strength and hardness are usually produced by quench and tempering, whereby the tempered martensite is the major constituent that provides surface hardness with enhanced wear resistance. Fracture toughness, which also contributes to fatigue life, represents the resistances against micro-crack initiation and growth. Obviously, grain boundary properties have profound effects on the initial stage of intergranular separations – the phenomenon presented in Fig. 1. Considering a carburized steel case as a system, the strength and fracture toughness of this system are determined by the combinations of the chemical composition, phase constituents and micro and sub-micro structural parameters. These parameters are mainly associated with the micro- and nano-scale heterogeneities; such as precipitates, solute atoms and second phase particles in grains, lattice misorientation and impurities segregation at grain boundaries, grain size and morphology, dislocations motions, and the interactions among them. From the viewpoints of strength and fracture toughness, these parameters can be distinguished into two classes: the heterogeneities inside a grain which determine the mechanical properties of the grain; and the complexities around grain boundaries which determine the interaction between adjacent grains; by the latter grain boundary adhesion is the dominant factor among others.

Hence, an intergranular fracture model is developed to investigate the failure process in the carburized steel case, which is illustrated in Fig. 2. In this diagram the macroscale crack is guided by the damage evolution within the small process zone in close vicinity around the crack tip. For intergranular fracture, evolution of damage and subsequent macro-scale crack growth are dominated by the decohesion process of grain boundary, because generally the martensite-phase-dominant grain is mechanically much stronger than the adhesion to adjacent grain at its boundary. This grain boundary decohesion is governed by the traction-separation law between to adjacent grains, as plotted at the upper right corner of the figure. The model in Fig.2 highlights grain boundary decohesion - the dominant mechanism of intergranular fracture. This decohesion essentially is a process to break the interatomic bond at quantum scales. Therefore, this model schematically establishes the correlations among macroscale crack growth, microscopic damage evolution and atomistic debonding. To obtain quantitative predictions of the strength and toughness of carburized steel case, the accurate computations in the following respects are necessary:

- grain boundary adhesion,
- Peierls' stress barrier and cleavage strength of grains,
- microscale constitutive modeling to integrate the effects of grain deformation and grain boundary decohesion,
- to embed the results of microscopic modeling into the macroscopic analysis of the damage-induced failure process.

In the following subsections the corresponding solutions will be introduced step by step.

The model presented in Fig. 2 provides a possibility to develop a multi-scale analytical tool for establishing the quantitative relationships among alloys and compounds selection, process design, microstructure optimization, and desirable properties for carburized steel case, as conceptualized by the flow chart in Fig. 3.

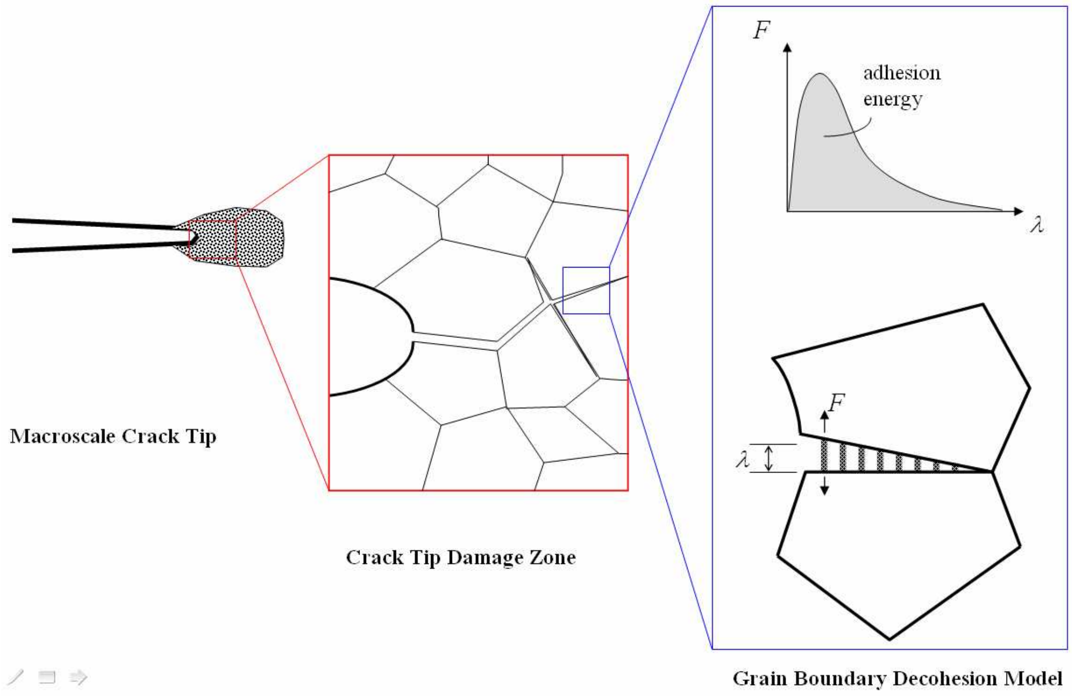

Fig. 2 A proposed multi-scale intergrannual fracture model

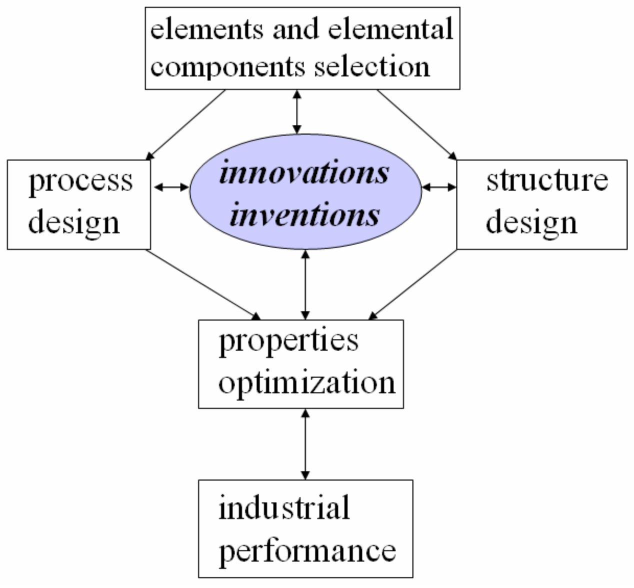

Fig. 3 The fundamental idea behind the proposed model in Fig. 2

2.2 Experiments

The uniaxial tension test and the compact tension test of fracture toughness for the AISI 8822 carburized steel have been conducted by Dana Corporation, following the ASTM Standard E8 and E399, respectively. The specimens have been fully carburized through entire thickness up to 0.91 pct carbon to represent the case part of a gear made of the steel, which is carried out with prolong duration of carburization to ensure carbon distributed uniformly through entire sample thickness. The tensile tests and fracture toughness tests were performed in normal laboratory environment at ambient temperature with no humidity control. Fracture toughness tests were conducted with the ASTM Standard Compact Tension specimens (CT) of thickness B: 5.08 mm, length W: 50.8 mm, and height: 60.96 mm. The microscopic observation indicates that the tempered martensite is the dominant constituent (>80%). The grain size is in the range of the ASTM E-112 size 9 with the average diameter of 16 microns. The measured mechanical properties and the chemical composition are listed in Tables I and II, where the tension strengths are measured at the uniaxial tension specimen after fully carburization.

Table I: Chemical Composition (wt%)

C	Mn	Ni	Cr	Mo	Cu	S	P	Si	Fe
0.91	1.01	0.51	0.57	0.30	0.15	0.0024	0.009	0.35	balance

Table II: Mechanical Properties

Young’s module (GPa)	Yielding Strength (MPa)	Ultimate Strength (MPa)	Engineering fracture strain (%)	Section reduction (%)
220	978	1369	13	2

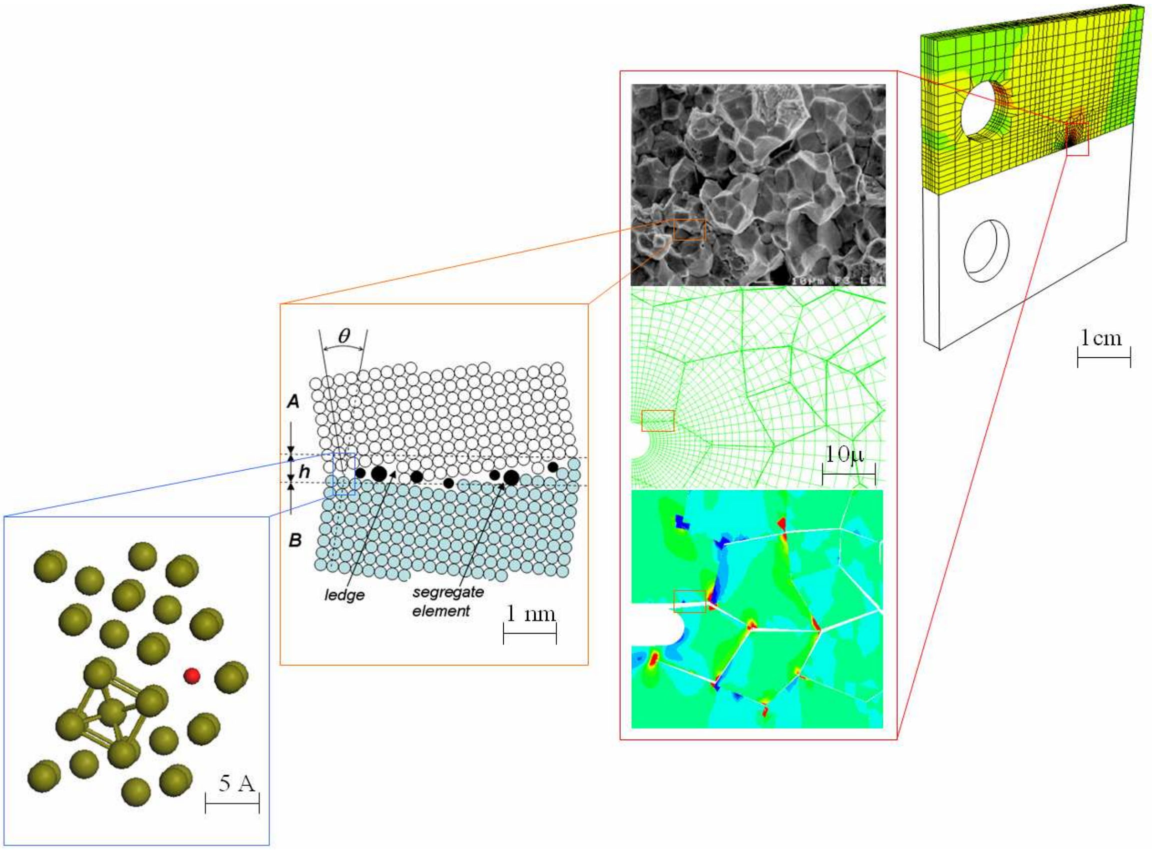

Fig. 4 An alternative expression of the multi-scale, multi-physic model of the intergranular fracture introduced by Fig. 2

2.3 A Bottom-Up Analysis Procedure

Fig. 4 details the procedure introduced by the model of Fig. 2. Starting at its right upper corner, a finite element model of the ASTM Standard CT specimen is plotted which is used to measure the conventional macroscale fracture parameters, such as CTOD (crack tip opening displacement), CMOD(crack mouth opening displacement), Stress Intensity Factor and J-integral. These parameters correlated to each other, defining a fracture toughness of the steel [39]. For carburized steels, the evolution of the crack tip damage zone is mainly dominated by the decohesion of grain boundary, as illustrated by Fig. 2. A numerical procedure, which is termed "Moving Particle Finite Element"(MPFEM) [25, 27, 30], is employed to integrate the deformation of grains and separation of grain boundaries through computation over the damage zone, as illustrated in the box left from the CT specimen. An intergranular decohesion can be mathematically described by the traction-separation relations between grain boundaries, which is similar to splitting an atomic array in bulk phase but with deducted adhesion energy due to localized concentration of heterogeneities, as illustrated in the plot left from the box of crack tip damage zone model. Hence, this traction-separation relation can be computed accurately by the sub-atomic quantum mechanical computations, e.g., on the primitive cell that is plotted at the left lower corner of the figure 4.

The aforementioned procedure can be outlined by the flow chart depicted in Fig. 5; the details for each part will be explained in the following sections. The numerical algorithms developed in [20, 25, 27, 30] have been applied in this procedure at various scales.

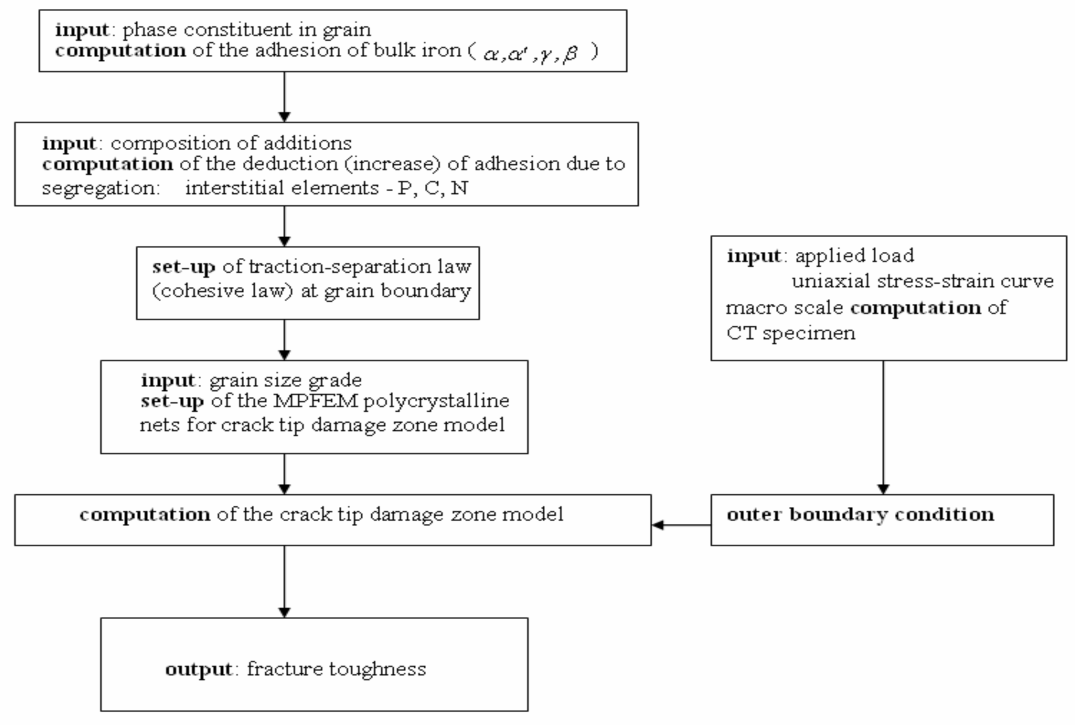

Fig. 5 A bottom-up procedure to perform the analysis and computations for the intergranual fracture model of carburized steel case introduced by Figs 2. and 4; where α, α', γ, and β refer to ferrite, martensite, austenite, and bainite phase, respectively.

2.4 Sub-Atomic Computation

2.4.1 Interfacial adhesion and Interatomic potential

Considering fracture as a split in an atomic array, the interfacial adhesion between the two separated surfaces governs the failure process of the material. On other hand, a fracture breaks bonded atoms pairs; the corresponding separation force is determined by interatomic potential. Obviously, the interaction between two neighbored atoms is not quantitatively identical to the adhesion between two adjacent atomic surfaces. The relationship in-between is crucial for establishing a hierarchical linkage in a multi-scale analysis, which is the issue to be clarified in this subsection.

Fig. 6 shows two chunks of atoms arrays, Ω_A and Ω_B, apart from each other with a distance λ_N. $T(\lambda_N)$, the attractive (or repulsive) force per unit area between the two paralleled surfaces S_A and S_B, can be expressed as the derivative of an interfacial cohesive potential $E^{coh}(\lambda_N)$ [26]:

$$T(\lambda_N) = \frac{\partial E^{coh}(\lambda_N)}{\partial \lambda_N}, \tag{1}$$

On other hand, let $f(r)$ be the interatomic force between two individual atoms *A* and *B* in Ω_A and Ω_B, respectively, with a distance *r*; and $E(r)$ be the corrresponding interatomic potential:

$$f(r) = \frac{\partial E(r)}{\partial r} \tag{2}$$

Assuming both Ω_A and Ω_B to be semi-infinite, the total force acting upon the single atom *B* from all atoms in Ω_A is:

$$f_B(\lambda) = n_A \int_{\Omega_A} \cos\theta \cdot f(r) d\Omega_A = n_A \int_0^{2\pi} r d\varphi \int_0^{\pi} 2r \cos\theta d\theta \int_{\frac{\lambda_N}{\cos\theta}}^{\infty} \frac{\partial E(r)}{\partial r} dr \tag{3}$$

where n_A is the number of atoms per unit volume in Ω_A. So the total traction/impulsion between the two bodies, represented by the adhesion $T(\lambda_N)$ between the surface pair S_A and S_B, yields

$$\frac{\partial E^{coh}(\lambda_N)}{\partial \lambda_N} = T(\lambda_N) = n_B \int_{unit\ area} dS \int_{\lambda_N}^{\infty} f_B(\lambda) d\lambda \tag{4}$$

where n_B is the number of atoms per unit volume in Ω_B.

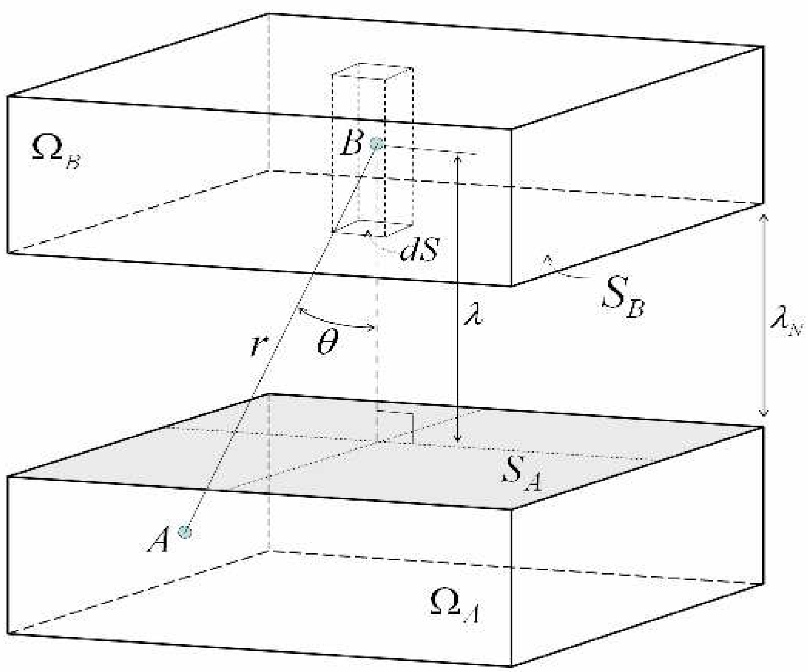

Fig. 7 The difference between interfacial adhesion and interatomic traction/repulsion: the normal traction/separation law between surfaces S_A of Ω_A and S_B of Ω_B is a function of the separation λ_N; whereas the cohesion between atoms *A* and *B* is determined by the interatomic distance *r* when omitting the effects of spin-polarization.

The equations (3) and (4) establish the analytical relationship between interatomic cohesion and interfacial adhesion. For example, quantum mechanics computation usually gives the interfacial adhesion potential E^{coh} between the opposite surfaces of two atomic slabs [26, 46]. When E^{coh} can be written as a polynomial as following:

$$E^{coh}(\lambda_N) = \frac{a_2}{(\lambda_N)^2} + \frac{a_8}{(\lambda_N)^8} + \frac{a_n}{(\lambda_N)^n} \dots , \qquad n \neq 2{,}8 , \tag{5}$$

where a_i , $i = 2{,}8{,}\dots$, are constant. By substituting (5) into (4) and (3) one finds that the corrresponding interatomic potential yields:

$$E(r) = 4\varepsilon_0 \left[\left(\frac{\sigma}{r} \right)^{12} - \left(\frac{\sigma}{r} \right)^{6} \right] \tag{6}$$

if

$$a_2 = -\frac{n_A n_B \varepsilon_0 \pi^3 \sigma^6}{2} , \quad a_8 = \frac{7 n_A n_B \varepsilon_0 \pi^3 \sigma^{12}}{256} \quad \text{and} \quad a_n = 0 \tag{7}$$

Eq.(6) is the conventional Lennard-Jones Potential for a biatom molecule system; where σ is the “collision diameter” that equals the separation when E is zero; ε_0 is related to the “well depth”, i.e. the minimum of E in the energy-separation (E, r) curve, which represents the equilibrium position:

$$f(r) = \left. \frac{\partial E(r)}{\partial r} \right|_{r=r_0} = 0 \qquad \text{and} \qquad r_0 = \sqrt[6]{2}\sigma$$

Thus, the first term on the right hand of (6) characterizes the repulse force when a pair atoms come closely ($r < r_0$); whereas the second term governs the traction when they separate away from the equilibrium position ($r > r_0$). It should be noticed that the bi-atomic potential (6) is under the approximation to omit the effects of hyperfine structure of atoms, although it has been widely applied for the computations of large molecular system,

Similarly to (1), the stress against sliding between two atomic surfaces, denoted as σ_T , is determined by the derivative of Peierls-Nabarro energy potential again stacking fault E_S [15, 20, 54]:

$$\sigma_T = \frac{\partial E_S}{\partial \lambda_T} \qquad \text{and} \qquad E_S = \gamma_{US} \sin^4\left(\frac{\pi \lambda_T}{b} \right) \tag{8}$$

where λ_T is the relative sliding; γ_{US} is the Peierls-Nabarro energy barrier against dislocation.

2.4.2 Geometrical discontinuities and grain boundary

In Fig. 6 the two adjacent surfaces S_A and S_B are parallel to each other but no assumption about the details, for example, lattice's orientations of Ω_A and Ω_B. Grain boundary essentially is accumulated discontinuities in a periodic distribution of atomic array, as categorized in Fig. 7. The discontinuities, in conjunction with impurities segregations, may reduce the grain boundary adhesion energies. To demonstrate the concept, in this paper only the tilted grain boundary in polycrystalline bcc iron system, i.e. the case (a), is taken into account, focusing on the effects of phosphorous segregation on fracture toughness. Obviously, the adhesion potential at grain boundary, denoted as E_{gb}^{coh}, will be different from the E^{coh} in bulk phase:

$$E_{gb}^{coh} = E^{coh} - \Delta E^{tilt} - \Delta E^{segragate} \tag{9}$$

where ΔE^{tilt} and $\Delta E^{segragate}$ are the deductions of adhesion energy due to tilt and impurities segregation, respectively. The similar expression also applies to the γ_{US} in (8), denoted as γ_{gb}^{US}.

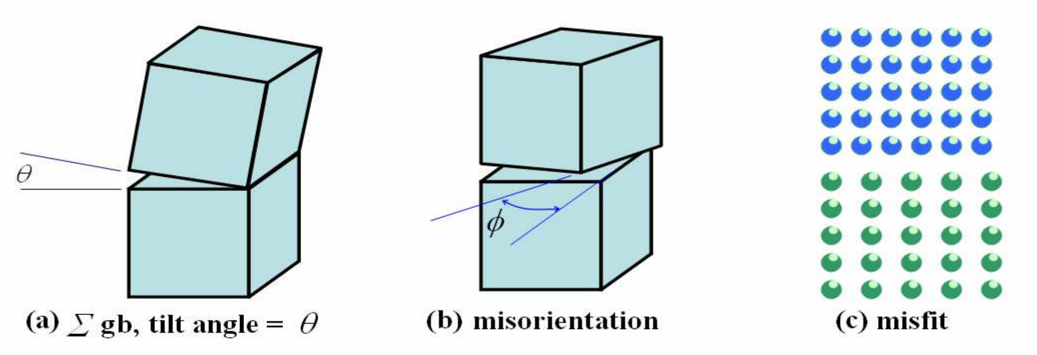

Fig. 7 Geometrical heterogeneities caused by grain boundary

2.4.3 Impuritie segregation

When chemical composition of a steel is known, an issue is to find how many the hazard elements, such as phosphorous and sulfur, segregated around grain boundaries. Let the symbol Γ_P^G to represent the weight percentage of phosphorous (P) segregated at grain boundary, the Langmuir-McLean model [17] gives an estimate of weight percentage of phosphorous at grain boundary:

$$\Delta\Gamma_P^G = \frac{1}{1 + x\,exp\left(\frac{\Delta G^0}{RT}\right)} \tag{10}$$

where $\Delta\Gamma_P^G$ is the increment of Γ_P^G during a heat treatment at a thermodynamic equilibrium state with the temperature T, ΔG^0 is the chemical potential of the corresponding bulk phase which is about -78 kJ/mol^{-1} (at 300K) [6], R is the universal gas constant and x is to be calibrated by test.

The equation (10) indicates phosphorous segregation can be controlled through adjusting heat treatment, which also provides a way to estimate Γ_P^G according to heat treatment history.

The experimental results of DANA Corp. have been used to calibrate the constant x. The range of Γ_P^G for the steel analyzed is below 10%.

2.4.4 DFT[2,3] Computation

In order to obtain E_{gb}^{coh} and γ_{gb}^{US} for establishing theoretical traction-separation law, the Density Function Theory[2,3] based quantum mechanics computations have been conducted, applying the full potential all electrons linear augmented plane wave (FLAPW) numerical codes [4, 44-46,71]. The procedure to set up periodic atomic supercells for this class of computations has been introduced in [4,70].

Fig. 7 indicates the types of geometrical discontinuities at grain boundary are enormous. Two kinds of atomic cells to model the grain boundaries with two tilted angles θ : $\Sigma 1 \left(\theta = 0^o\right)$ and $\Sigma 5 \left(\theta = 51.13^o\right)$, are computed at ground state. The $\Sigma 1$ grain boundary is the case that two adjacent grains have the same lattice's orientation but with phosphorous segregation in-between, which is a degenerated case of low-angle grain boundaries. When this is no segregation, it becomes a bulk crystal. The primitive cell of $\Sigma 5$ grain boundary is given by the plot on the left hand side of Fig. 8, which is a typical high angle grain boundary. The corresponding distributions of electron charge density for the boundary cell and $\Sigma 5$ surface, respectively, are plotted on the right hand side of the figure. Applying the procedure introduced in [26, 32, 20], the differences between them and those without phosphorous segregation define the $\Delta E^{segragate}$ whereas the difference between non-segregation $\Sigma 1$ and $\Sigma 5$ define the ΔE^{tilt} caused by $\Sigma 5$ tilt in (9). Grain boundaries with other tilted angles less than $\left(\theta = 51.13^o\right)$ are interpolated between zero and the ΔE^{tilt} of $\Sigma 5$. The twin boundary is not taken into account for the intergranular fracture studied.

The computed adhesion energies for bulk bcc iron and for the $\Sigma 1$ grain boundary with phosphorous segregation are plotted in Fig. 9a, by which the discretized numerical data were fitted into polynomials (5-7). As expected, a remarkable drop in adhesion energy can be seen when P segregate presents. For the $\Sigma 5$ boundary ΔE^{tilt}, the reduction of adhesion energy, is about 18% when $\Gamma_P^G = 0$. Considering grain boundary represents a "discontinuity" of periodic array of atoms, the reasons that cause the drop of adhesion energy can be: (i) the segregated interstitial phosphorous atoms weaken metallic Fe-Fe bonds; (ii) the tilted boundary is actually an array of empty sites that enlarges the interatomic distance between the atoms from adjacent grains; (iii) segregated P atoms or titled boundary breaks the periodicity in bulk phase, which alternates the ferromagnetic alignment of bcc iron and, thus, induces localized antiferromagnetic-like spin-polarization (see Fig. 9b); it is well-known that the iron fcc crystal is antiferromagnetic, which is with less stability as compared with bcc iron, see Appendix I. Table III lists the computed values of E^{coh}, ΔE^{tilt} and $\Delta E^{segragate}$. Results of other segregations or grain boundary tilt angles can be found, e.g. in [6,10,11,31,32]. According to the computation in [20]: $\gamma_{US} \approx 0.43$ (J/M^2). At grain boundary the relation $\gamma_{US}^{gb} = \gamma_{US} \left(E_{gb}^{coh} / E_{gb}\right)$ is applied in this analysis.

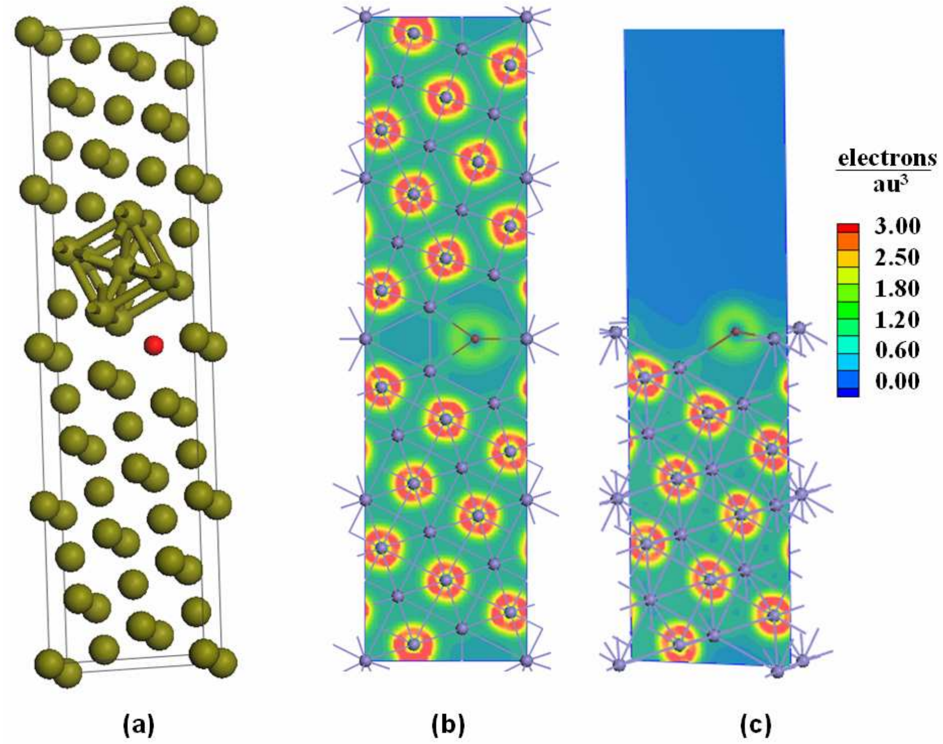

Fig. 8 The supercell of $\Sigma 5$ bcc iron grain boundary with phosphorous segregate (a) and charge density in the middle layer of the cell (b, c); where the red ball in (a) and the small dark-gray ball in (b) and (c) are Phosphorous atoms whereas the others are iron atoms; a bcc cell is illustrated in in the supercell of (a). The misorientation defined by Fig. 7 is zero in these computations.

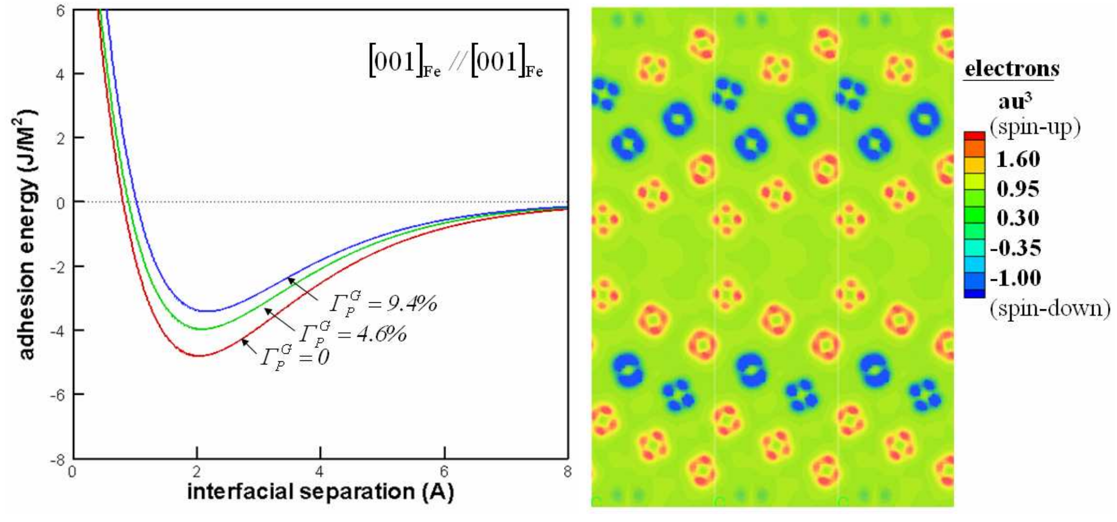

(a) grain boundary adhesion energies

(b) spin-charge density around $\Sigma 5$ grain boundary without phosphorous segregation; it demonstrates a semi-periodic distribution in vertical direction which is somewhat like that presented in anti-ferromegnetic fcc; from the horizontal periodicity one sees that the computation is performed using the cell of Fig. 8(a).

Fig. 9. Computation of the grain boundary adhesion with phosphorous segregation

Table III Grain boundary adhesion energy for BCC iron (J/M^2)

E^{coh}	$\Delta E^{tilt}(\sum 1)$ $\Gamma_P^G = 0$	$\Delta E^{tilt}(\sum 5)$ $\Gamma_P^G = 0$	$\Delta E^{segragate}(\sum 1)$ $\Gamma_P^G = 4.6\%$	$\Delta E^{segragate}(\sum 1)$ $\Gamma_P^G = 9.4\%$
4.97	0	1.67	0.94	1.61

where *P*: phosphorous; Γ_P^G : weight percentage of *P* segregation

2.5 A Hierarchical Multi-Scale Procedure

A major challenge for the object studied is to bridge the sub-atomic computation with micro and macro analysis, which requires a hierarchical scheme to integrate the kinetics from angstroms to centimeters while highlighting the dominant mechanisms. This is somewhat different from many recently developed successful methods, for examples, [57-63]. In order to predict the steel's fracture toughness, the following two steps are vital important: (I) implement the results of quantum mechanical computation obtained in the previous subsection into the polycrystalline system; (II) to embed the information of grain-sized analysis into the inch-sized fracture toughness specimen, so as to compute the macro-scale parameters that characterizes material's fracture.

2.5.1 Sub-Atomic to Up-atomic

The step I mentioned above requires to bridge the sub-atomic quantum physics with up-atomic continuum analysis. As plotted in the flow chart of Fig. 5, the Moving Particle Finite Element Method (MPFEM) is employed for this purpose. It contains the methodologies in two perspectives: finite element and particle method. For sub-atomic to up-atomic bridging, the 'Particle Dynamics', introduced in [20,28], is applied to the step I. The idea of this approach is to represent an atomic system as a particle system through lumping several atoms into a super-atom, termed "particle", while preserving the essential properties of the atomic system via a proposed "equivalent stiffness rule". This rule requires that the particle system has the same periodic structure and stiffness as the original system but with a larger inter-particle spacing that is determined according to the scale of interest, see Figs. 10a,b. The sub-atomic physics, which may dominate the mechanical behavior at up-atomic scales, is preserved through transforming the inter-atomic potential into an inter-particle potential by the following way:

Assuming E^{atom} to be the interatomic potential, like (6), for the system in Fig. 10a., when it is suffering a deformation, for example, a_0 becomes a_1; accordingly $R \to R_1 = Na_1$ in the particle system of Fig. 10b. This deformation can be represented by a uniform strain field ε_{ij} for both systems. The corresponding stress tensor σ_{ij}^{atom} and stiffness tensor C_{ijkl}^{atom} of the atomic system yield [26, 56]:

$$\sigma_{ij}^{atom} = \rho\left(\frac{\partial E^{atom}}{\partial \varepsilon_{ij}} - 2\varepsilon_{ik}\frac{\partial E^{atom}}{\partial \varepsilon_{kj}}\right) \tag{11a}$$

and

$$C_{ijkl}^{atom} = \frac{\partial \sigma_{ij}^{atom}}{\partial \varepsilon_{kl}} \tag{11b}$$

where ρ is density and the dummy summation rule is applied. The second term on the right hand side of (11a) is corresponding to finite strain [56], which can be omitted when deformation is small.

Similarly, for the particle system in Fig. 10b with an inter-particle potential $E_{Particle}$:

$$\sigma_{ij}^{Particle} = \rho\left(\frac{\partial E_{Particle}}{\partial \varepsilon_{ij}} - 2\varepsilon_{ik}\frac{\partial E_{Particle}}{\partial \varepsilon_{kj}}\right) \tag{12a}$$

and

$$C_{ijkl}^{Particle} = \frac{\partial \sigma_{ij}^{Particle}}{\partial \varepsilon_{kl}} \tag{12b}$$

The "equivalent stiffness rule" requires:

$$C_{ijkl}^{Particle} = C_{ijkl}^{atom} \tag{13}$$

which leads to

$$\sigma_{ij}^{Particle} = \sigma_{ij}^{atom} \tag{14}$$

The equality (13) provides a group of conditions to determine $E_{Particle}$ that gives the same stresses for both systems, as confirmed by (14). However, the computational effort by Particle Dynamics is reduced to about $1/N^m$ of that by atomic system for a *m*-dimensional case; where *N* defines the size of the particle, see Fig. 10b, and *m*=1,2,3. An analysis of the bcc iron lattice with grain boundary is given in [20, 28].

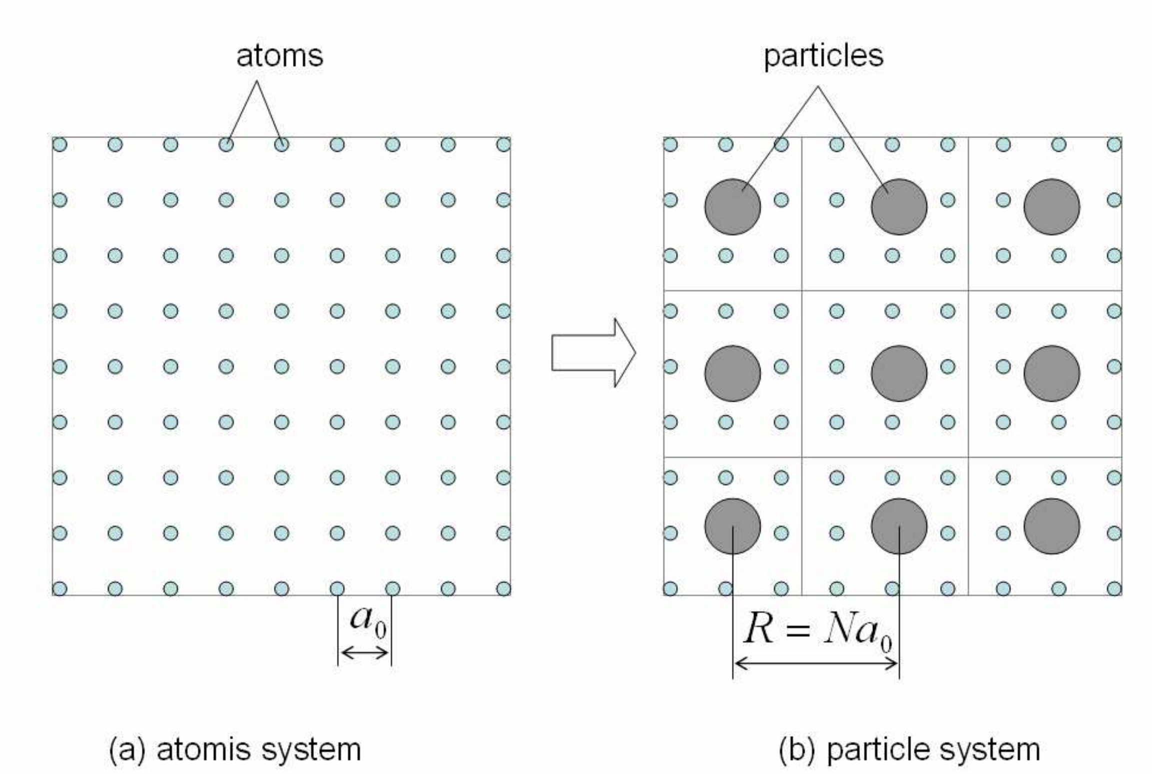

Fig. 10 The "Particle Dynamics" method [20] that transfers the atomic system (a) into the particle system (b) through segregating the atoms within the cell of dimension *R* into a particle whereas an "equal stiffness rule" is imposed to ensure the two systems having the same elastic properties.

According to the procedure introduced above, one can find that as compared with other successful multiscale methods, e.g. the Quasicontinuum [60, 61], the novelty of the Particle Dynamics lies in the following two perspectives:

- The Particle Dynamics (PD) is a "hierarchically-structured" method to transfer an atomic system into a particle network that keeps the same lattice structure as the original; by contrast, in the methods of [58, 60,61] a finite element contains a set of atoms and the finite element net work may have the slip motion that differs from the particle network.
- The "equivalent stiffness rule" of Particle Dynamics provides a unique way to reproduce an inter-atomic interactions as an inter-particle interaction while preserve the origin of mechanical interatomic interaction at mesoscopic level.

Applying this approach, the quantum mechanical computation-based interfacial adhesions are applied to describe the grain boundary traction-separation relation for the polycrystalline system that plotted in the second column from right in Fig. 4, where each grain is a crystal made of "particles" which are segregations of atoms. The traction-separation relation has been implemented into a group of "cohesive elements" that connect each grain boundary surfaces pair, e.g. the *AB* in Fig. 11a. On other hand, all grains are treated as bcc crystals with the same [001] direction perpendicular to the two-dimensional plane but randomly pre-assigned in-plane orientation. Each particle in a grain defines a "node", the connections among these nodes form small finite elements that partition the grain. The finite element is with the average size about one order smaller than average grain size, as illustrated in the middle box of the second column from right in Fig. 4. The finite elements obey the constitutive relation of crystal plasticity with Taylor's hardening (isotropic hardening) [18]; which is governed by the effective stress-strain relation that is calibrated according to the quantum mechanics analysis of bulk iron phase through the "Particle Dynamics" method, as described in [28]. The Moving Particle Finite Element method [25,27,30], which integrates all atomic segregates into a polycrystalline network that combines the "cohesive elements" and grain finite elements, has been applied for the micro-scale computation.

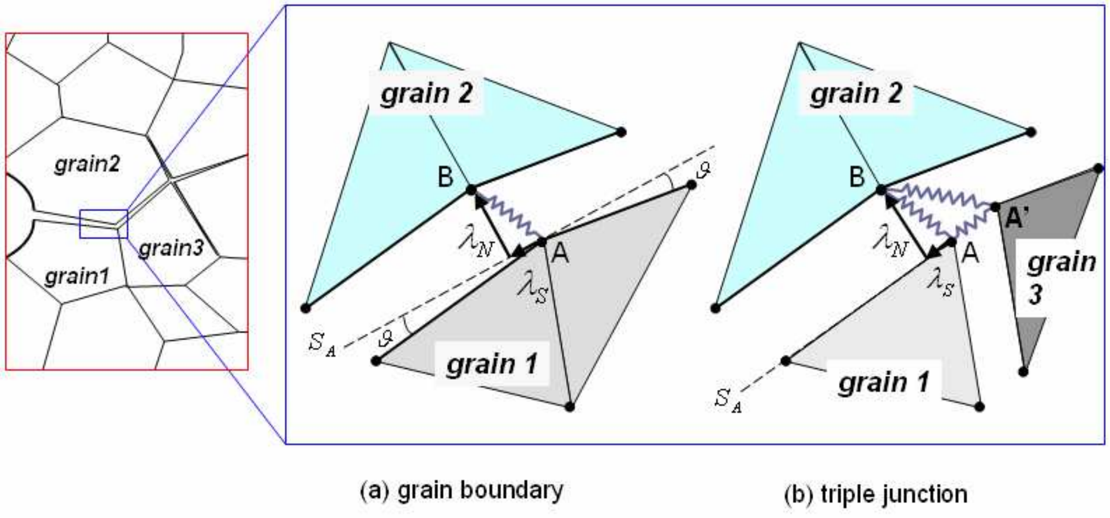

Fig. 11 MPFEM cohesive elements for the computations of grain boundary separation and sliding; (a) the cohesive element *AB* connects two adjacent grains that are descritized by the finite elements associated with points *A* and *B*; where S_A is the "master surface" enhanced to the node *A* in numerical analysis, defining the normal separation λ_N and relative sliding λ_S, respectively; thus, the grain boundary surface associated with node *B* is defined as "slaver surface"; (b) at triple junction the three cohesive elements, i.e. *AB*, *AA'*, *A'B*, and corresponding master-slaver surfaces pair, are required in analysis. Moving Finite Element Method [25, 27, 30] is applied to integrate cohesive elements and grains.

2.5.2 Micro to Macro Scale

As mentioned in the previous subsection, the size of finite element inside a grain is in the order of micron; for a grain by grain micro-structured two-dimensional computation of a ASTM standard CT specimen, a model with about 6.25×10^{11} finite elements (10^{17} elements for 3D) is required. Obviously, more effective scheme will be preferred since the damage caused by intergranular cracking is limited only within the close vicinity of the crack tip; the rest part of the specimen can be described by well-developed theory of isotropic and uniform plasticity; for the latter, finite element with the size of millimeter is sufficient.

In this analysis a scheme is developed by which the CT specimen is divided into two parts: a small chunk of material surround the crack tip which is modeled by the polycrystalline microstructure; an example of this crack tip zone, denoted as Ω_t, is plotted on the right upper corner of Fig. 12. The rest part of the specimen, denoted as Ω, is modeled by the continuum J_2 flow plasticity theory using regular finite element. The external load applied to the specimen is transferred into the crack tip through the continuity conditions of traction $\boldsymbol{T}$ and displacement $\overline{\boldsymbol{u}}_t$ on the shared boundary Σ. The detail of the three-dimensional meshes around Σ in Ω is given by Fig. 12, which shows the adoption from the relatively small finite elements near Σ to the coarse elements away from it. $\boldsymbol{T}$ and $\overline{\boldsymbol{u}}_t$ at the Σ on the middle section of the 3D block define the plane strain boundary condition on the Σ of Ω_t. This is similar to the "boundary layer method", e.g., in [37], by which the stresses of asymptotic analytical solution, such as mode-I K-field [39], is applied to the outer boundary of crack tip zone.

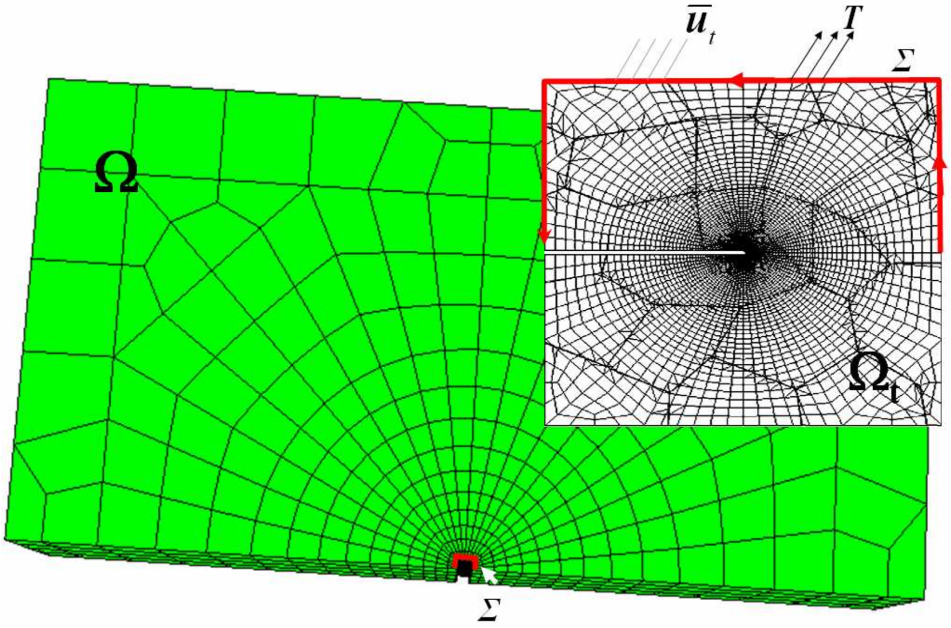

Fig. 12 The developed scheme divides a standard specimen into two parts: the polycrystalline slab Ω_t containing, for example, a sharp crack tip, as plotted on the right upper corner; which "shakes" hands to the rest of the specimen through the continuities of displacement and J-integral on the boundary Σ

However, when massive microscale intergranular cracks occur within Ω_t, the stresses on Σ may decrease due to material's softening while $\overline{\boldsymbol{u}}_t$ still increases. In other word, the traction $\boldsymbol{T}$ alone does not uniquely determine the deformation field inside Ω_t. By contrast, the $\overline{\boldsymbol{u}}_t$ on Σ is monotonic when external load in the form of displacement increases monotonically. Generally it is very difficult to satisfy the both stress and displacement continuities simultaneously by boundary layer method; instead, a *J*-integral[13] based "shake hand" scheme is developed which requires the satisfaction of the continuous conditions of displacement and *J*-integral on Σ; the latter represents the energy that flows into the crack tip.

This "shake hand" scheme includes three computations: beside the computation of the part Ω and that of the polycrystalline system Ω_t with intergranular cracking, respectively, the third computation of the entire specimen ($\Omega_t + \Omega$) is conducted by which no intergranular cracking in Ω_t, so all material are obeying the same plasticity law. The quantities associated with these three computations are distinguished in turn by the superscriptions Ω, Ω_t, and $\Omega_t + \Omega$.

Then, for the two cases without intergranular cracking, the corresponding *J*-integral, applied load *P*, and CMOD (crack mouth opening displacement) *U* are $J^{\Omega}, P^{\Omega}, U^{\Omega}$ and $J^{\Omega_t+\Omega}, P^{\Omega_t+\Omega}, U^{\Omega_t+\Omega}$, respectively. The reason for the third computation is to find the external load ($P^{\Omega_t}_{damage}$) and CMOD ($U^{\Omega_t}_{damage}$) corresponding to the computation of Ω_t with intergranular cracking induced damage.

The displacement on Σ obtained from the third computation, denoted as $\bar{\boldsymbol{u}}_t^{\Omega_t+\Omega}$, is used as the boundary condition imposed on Σ for the computation of the polycrystalline system Ω_t with intergranular cracking, which leads to the corresponding *J*-integrals J^{Ω_t} on Σ. On other hand, a reference crack tip opening displacements (CTOD), $\bar{u}_{CTOD}$, defined as the integral over Σ of the vertical component of $\bar{\boldsymbol{u}}_t$ with respect to *dx* and then divided by the length of the projection of Σ on the horizontal coordinate *x*, is recorded for all three computations. For a given $\bar{u}_{CTOD}$: $P^{\Omega_t+\Omega} > P^{\Omega}$, $U^{\Omega_t+\Omega} \cong U^{\Omega}$, and $J^{\Omega_t+\Omega} > J^{\Omega_t} > J^{\Omega}$. So $P^{\Omega_t}_{damage}$, the corresponding external load to the computation of Ω_t with intergranular cracking, is obtained through the following interpolation:

$$P^{\Omega_t}_{damage} = P^{\Omega} + \left(P^{\Omega_t+\Omega} - P^{\Omega}\right)\frac{J^{\Omega_t} - J^{\Omega}}{J^{\Omega_t+\Omega} - J^{\Omega}} \tag{15}$$

which is the load that is actually applied to the specimen. This procedure is under the approximation that the displacement field in Ω changes monotonically when the CT specimen is under a monotonic load in the type of load-line displacement. This is a reasonable approximation for small-scale yielding.

Hence, the applied load to the CT specimen induces macro-scale crack mouth opening displacement (CMOD), which links to the micro-scale computation on the polycrystalline slab Ω_t through the shared displacement boundary condition and consistency in J-integrals. This two-level computational scheme reproduces the processes of macro-scale crack growth-induced fracture based on the simulation of the damage evolution caused by grains, grain boundaries' sliding and separation in the local area surround the crack tip and the deformation in entire specimen; which enables the quantitative predictions of the relationships among fracture toughness, applied load, grain, grain size, grain boundary adhesion, and the associated sub-atomic physics, as illustrated by the flow chart in Fig. 5.

3. RESULTS AND DISSCUSION

Fig. 13 is a set of snap-shots of the evolutions of stress field in the damage zone Ω_t surrounding a blunted crack tip of the CT specimen, when applied load increases and the corresponding grain boundary separation occurs in Ω_t. Fig. 14 gives the comparison between the simulated load-CMOD relation and experimental results. Fig. 15 shows the computed fracture toughness according to ASTM E399 when the content of phosphorous varies. As expected, higher content of phosphorous leads to lower fracture toughness within the range computed.

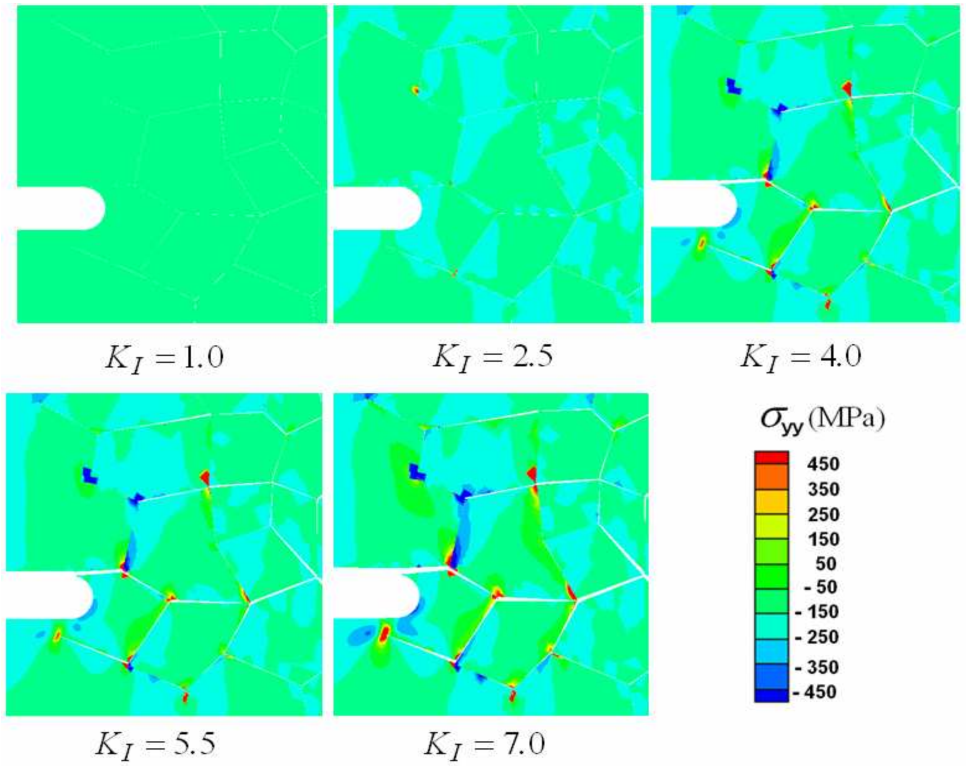

$K_I = 1.0$ $K_I = 2.5$ $K_I = 4.0$

$K_I = 5.5$ $K_I = 7.0$

Fig. 13 Intergranual fracture – MPFEM microscale simulation for the case with blunted crack tip

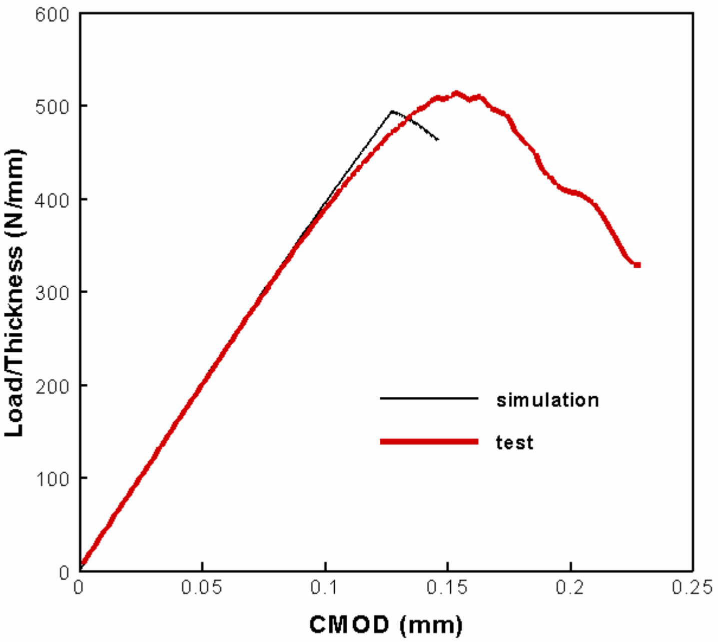

Fig. 14 The computed Load-CMOD curves for the specimens with different weight percentages of phosphorous

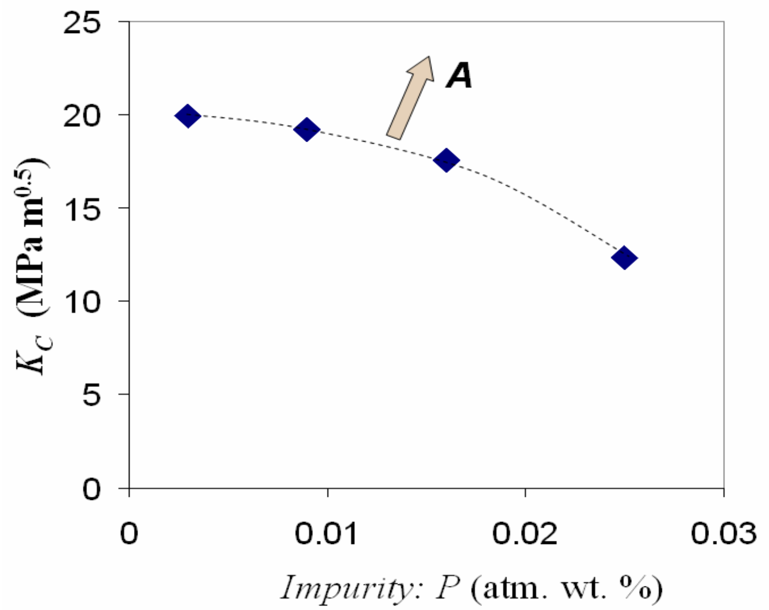

Fig. 15 The relationship between fracture toughness and the content of phosphorous, computational results , by improving grain ductility, the curve may move up, as indicated by the arrow A.

It is no doubt that phosphorous segregates will embrittle metal. However, by comparing the drop in fracture toughness plotted in Fig. 15 and the deduction of adhesion energy plotted in Fig. 9a when phosphorous increases, the changes in the former is much more significant than that in the latter. This can be explained by the simulations in Fig. 13, which shows a severe stress concentration at triple-junctions and the junctions of multi-grain boundaries when the average amplitude of the stress field is moderate. Thus, each junctions becomes a source of microscale-cracking, which causes decohesion along grain boundaries. The accumulation of these microscale-cracks forms a damage zone ahead a macro-scaled crack tip. The evolution of this damage zone leads to the subsequent macroscale crack growth. Consider a material is a system, an intergranual fracture essentially is the result of the interaction between grain boundary separation and deformation of grains. Therefore, removing the stress concentration at junctions of grain boundaries and increasing grain boundary adhesion are the two equally important goals for improving the mechanical properties of the steel. The study conducted inspires the ideas to achieve the first goal by increasing grain ductility through alloy additions, e.g. Ni, and phase constituents, e.g. with optimized ratio of bainite and retard austenite; while to improve grain boundary properties through the following two ways: (i) adding grain boundary clue elements such as B and Nb; which also have the function to pin grain boundary so reduce grain’s size; (ii) alloying with appropriated processing to promote the formations of $(M, P)_xC_y$ and $(M, S)_xC_y$ compounds which extract P and S out from grain boundaries.

4. Conclusions and Suggestions

From the viewpoint of mechanical analysis, this paper reports an effect to understand the intergranular fracture phenomenon in polycrystalline system based on the underlying fundamental physics. A hierarchical, multi-scale procedure has been developed through quantitatively integrating the information obtained from a series of density function theory-based computations to the corresponding micro and macro-scale particle-finite element analysis. This procedure has been applied to an analysis of AISI 8822 carburized steel case to explore the possibilities of improving toughness while sustaining desirable strength and wear resistance. This analysis concludes that for the studied polycrystalline system consisting of grains with high hardness and strength, an intergranular fracture is governed by the interaction of grain boundary adhesion and stress concentration at triple and other multiple grain boundaries' junctions. Hence, optimized mechanical properties for this class of steels can be achieved through the following conventional ways:

- Refine grain size: although finer grains may be detrimental to toughness, however, when the average size is not less than 10^2 nm, smaller grains may reduce the local resistance against dislocation motion around grain boundaries-junction while increase the energy barriers against large scale yielding due to increased zigzag in slipping paths, which elevates the strength of an alloy according to conventional Hall-Petch relation. Also, finer grains enlarge the total area of grain boundaries which reduces average impurities segregation per unit area of grain boundary. Hence, the trade-off of these factors may finally lead to a positive effect to the system.

- Alloying and processing to simultaneously improve grain boundary adhesion and grain's ductility: high grain's ductility reduces the stress concentration at triple-junctions; a summation of these two mechanisms may result in the transition from intergranular fracture to trangranular fracture.

Appendix

In the following text boldface symbol denote tensor, the order of which is indicated by the context. Plain symbols denote scalars or a component of a tensor when a subscript is attached. Repeated indices are summed. For two order tensors $\boldsymbol{a}$ and $\boldsymbol{b}$, $\mathbf{a} = \left[a_{ij}\right]$, $\mathbf{b} = \left[b_{ij}\right]$; then $\boldsymbol{a}^T = \left[a_{ji}\right]$, $\mathbf{a} \cdot \mathbf{b} = \left[a_{ik} b_{kj}\right]$, $\mathbf{a} : \mathbf{b} = \left[a_{ij} b_{ij}\right]$, and $\mathbf{ab} = \left[a_{ij} b_{kl}\right]$.

I Feromagnetic and Antiferromagnetic phases of Iron [65]

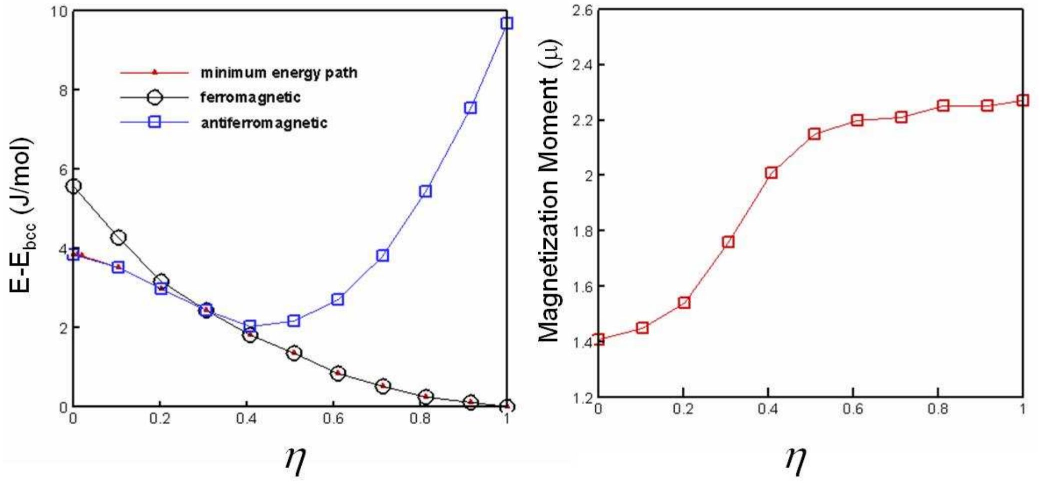

(a) (b)

Fig. A1: (a) Comparison of the ground state ferromagnetic and antiferromagnetic system energies of unit atomic cell when it transforms from bcc to fcc crystal along "Bain path"; where η is the order parameter to characterized the lattice constant ($\eta = 0$: fcc, $\eta = 1$: bcc); so the fcc crystal has antiferromagnetic structure with higher ground state energy than bcc. (b) The magnetization moment per atom when the lattice structure varies along Bain path.

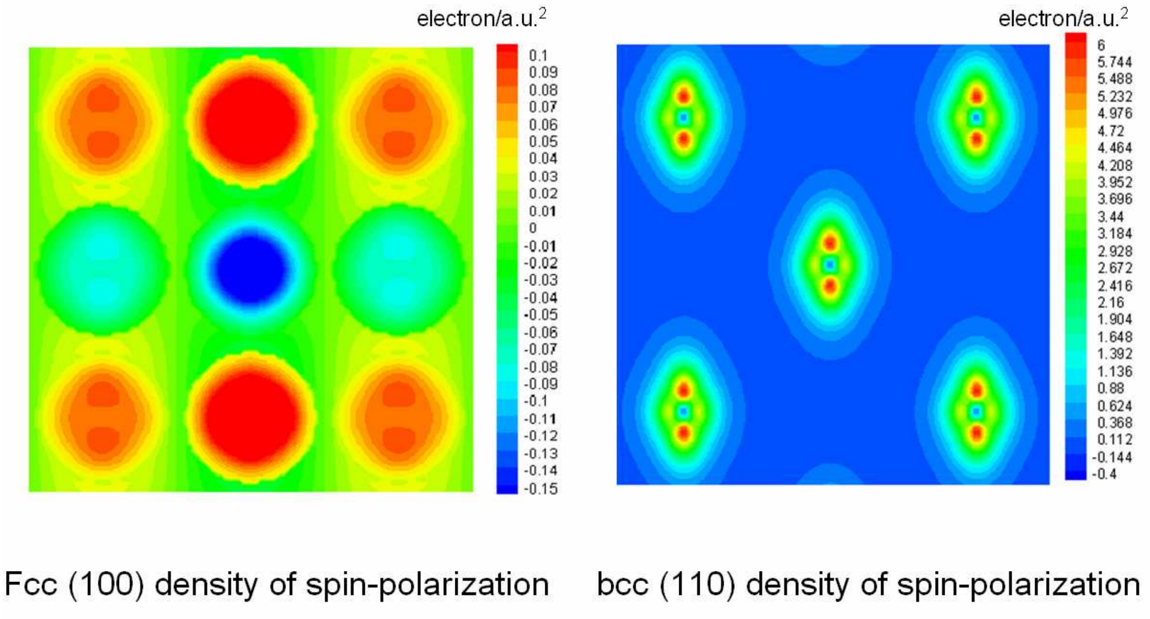

Fig. A2: Spin-charge density distributions for bulk fcc (left) and bcc (right).

II: About the "Moving Particle Finite Element Method" (MPFEM) [25, 27, 30]

The network that connects all particles obtained from "Particle Dynamics"[20] forms a finite element mesh, which is the same as the mesh that represents a discretized body in solid mechanics finite element analysis [50-53]. Fig. A3(a) shows an example of such a solid body Ω with the boundary $\partial\Omega_t$ of force boundary condition (natural boundary condition) and $\partial\Omega_u$ of displacement boundary condition(essential boundary condition). It has been partitioned into 9 triangle elements in (b). Each corner of a triangle element is a particle that is termed "node" in finite element analysis. In the i^{th} element, the strain incremental tensor inside a finite element, denoted as $\Delta\boldsymbol{\varepsilon}$, is expressed as the function of the displacement increments vector $\Delta\boldsymbol{u}_i$ at all nodes associated with this element:

$$\Delta\boldsymbol{\varepsilon} = \boldsymbol{B}_i \cdot \Delta\boldsymbol{u}_i \qquad \text{(b1)}$$

where the rule of dummy summation for the repeated index i applies; $\boldsymbol{B}_i$ is the "differential matrix", determined by displacement-strain relation (e.g. Cauchy geometric relation) and the interpolation scheme (shape function) of the finite element.

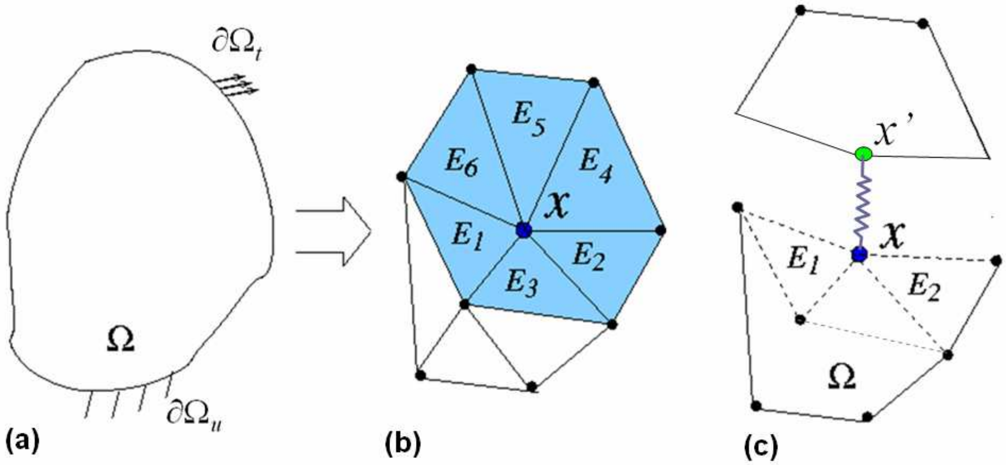

Fig. A3: The conception of MPFEM applied to grain boundary with cohesive element *xx'*;

Assuming that the elements E_1, E_2, E_3 belong to one grain while E_4, E_5, E_6 belong to another grain, then the node between two grains actually is a "cohesive element" that connects the particles from two adjacent grains' surfaces; for example, the x and x' in Fig. A3(c). The "Moving Particle Finite Element Method" [25,27,30] is able to solve the equilibrium condition at nodes through the virtual work principle.

Considering the node $\boldsymbol{x}$ in the case of Fig. A3(b), the virtual work principle-based equilibrium condition at this node implies that the work done by a force $\Delta \boldsymbol{F}_x$ imposed on the nodal $\boldsymbol{x}$, which is the product of $\Delta \boldsymbol{F}_x$ and a virtual nodal displacement $\Delta \boldsymbol{u}_x$ at this node, equals the summation of the strain energies caused by $\Delta \boldsymbol{u}_x$ in all elements shared the node $\boldsymbol{x}$:

$$\Delta \boldsymbol{F}_x \cdot \Delta \boldsymbol{u}_{\boldsymbol{x}} = \sum_{i=1}^{6} (\Delta \boldsymbol{\sigma} : \Delta \boldsymbol{\varepsilon}) V_i = \sum_{i=1}^{6} (\Delta \boldsymbol{\sigma} : \boldsymbol{B}_i \cdot \boldsymbol{\Delta \bar{u}_i}) V_i \tag{b2}$$

where V_i is the volume of the i^{th} element; $\boldsymbol{\Delta \bar{u}_i} = [\boldsymbol{\Delta u_x}, \boldsymbol{0}]^T$ is a vector that contains the displacement increments at all nodes associated with the elements adjacent to the node $\boldsymbol{x}$; but by the virtual work principle it is assumed all these nodal displacements are zero except $\Delta \boldsymbol{u}_x$; $\Delta \boldsymbol{\sigma}$ is the stress increment tensor that is correlated to $\Delta \boldsymbol{\varepsilon}$ through the constitutive law:

$$\Delta \boldsymbol{\sigma} = \boldsymbol{C}_t : \Delta \boldsymbol{\varepsilon} \tag{b3}$$

where $\boldsymbol{C}_t$ is the tangential stiffness matrix of the bulk phase, which is a fourth order tensor.

In MPFEM there is no restriction to the type of the elements in the nodal equilibrium condition (b2). For the case in Fig. A3(c) the node *x* is at a grain boundary formed by the upper edges of the triangle elements E_1 and E_3. The developed cohesive element *xx'* establishes the connection between the two sides of the opposite grains. Similar to (b2), the equilibrium condition at the node $\boldsymbol{x}$ can be expressed as the following summation.

$$\Delta \boldsymbol{F}_x \cdot \Delta \boldsymbol{u}_x = \sum_{i=1}^{3} \left(\Delta \boldsymbol{\sigma} : \boldsymbol{B}_i \cdot \Delta \bar{\boldsymbol{u}}_i\right) V + \Delta \boldsymbol{F}_x^{decoh} \cdot \Delta \boldsymbol{u}_x^{decoh} \tag{b4}$$

where $\Delta \boldsymbol{F}_x^{decoh}$ and $\Delta \boldsymbol{u}_x^{decoh}$ are the force and elongation vector of the cohesive element; when there is no displacement on the other end of the cohesive element:

$$\Delta \boldsymbol{u}_x^{decoh} = \Delta \boldsymbol{u}_x = \left[\lambda_N, \lambda_S\right]^T . \tag{b5}$$

where λ_N and λ_S are the normal and tangential separation in (1) and (8), respectively.

When all other nodes are fix but node *x* has the displacement $\Delta \boldsymbol{u}_x$, one can remove $\Delta \boldsymbol{u}_x$ from the both sides of (b4), which becomes the equilibrium condition at this node in matrix form:

$$\Delta \boldsymbol{F}_x = \tilde{\boldsymbol{K}} \cdot \Delta \boldsymbol{u}_x \tag{b6}$$

where $\tilde{\boldsymbol{K}} = \boldsymbol{K}_t + \boldsymbol{K}_{decoh}$; the grain matrix tangential stiffness $\boldsymbol{K}_t$ and decohesion stiffness $\boldsymbol{K}_{decoh}$ are defined as below:

$$\boldsymbol{K}_t = \sum_{i=1}^{3} \left(\boldsymbol{B}_i^T : \boldsymbol{C}_t : \boldsymbol{B}_i\right) \cdot V \tag{b7}$$

and

$$\boldsymbol{K}_{decoh} = \frac{\partial\left(E^{coh}, E_S\right)}{\partial\left(\lambda_N, \lambda_S\right)} \tag{b8}$$

References

1. Slater, J. C.., *Quantum Theory of Atomic Structures.* McGraw-Hill, New York, 1960.

2. Hohenberg, P., Kohn, W., *Inhomogeneous Electron Gas.* Physical Review, 1964. **136**(3B): p. 864-871.

3. Kohn, W., Sham, L. J., *Self-Consistent Equations Including Exchange and Correlation Effects.* Physical Review, 1965. **140**(4A): p. 1133-1138.

4. Freeman, A.J., *Materials by design and the exciting role of quantum computation/simulation.* Journal of Computational and Applied Mathematics, 2002. 149(1): p. 27-56.

5. Olson, G.B., *Computational design of hierarchically structured materials.* Science, 1997. 277(5330): p. 1237-1242.

6. Rice, J.R. and J.S. Wang, *Embrittlement of Interfaces by Solute Segregation.* Materials Science and Engineering a-Structural Materials Properties Microstructure and Processing, 1989. 107: p. 23-40.

7. McLean, D., *Grain Boundaries in Metals*. 1957, Oxford: Oxford University Express.

8. Weertman, J., *Theory of fatigue crack growth based on a BCS Theory with work hardening*. 1973, Int. J. Fracture, 9(2), p. 125-131.

9. Hutchinson, J.W., *Bounds and Self-Consistent Estimates for Creep of Polycrystalline Materials.* Proceedings of the Royal Society of London Series a-Mathematical Physical and Engineering Sciences, 1976. 348(1652): p. 101-127.

10. Hill, R., *Mathematic Theory of Plasticity*, Cambridge Express, 1951.

11. Feynman, R. P., *Forces in Molecules.* Physical Rev., 1939. 56: p. 340-343.

12. Morse, P. M., *Diatomic Molecules Approaching to the Wave Mechanics II. Vibrational Levels.* Physical Rev., 1929. 34: p.57-63.

13. Rice, J. R., *A Path Independent Integral and Approximation Analysis of Strain Concentration by Notches and Cracks.* J. Appl. Mech., 1968. **35**(2): p. 379-386

14a. Hutchinson, J. W., *Singular Behavior at the End of a Tensile Crack in a Hardening Material*, J. Mech. Phys. Solids, 1968,. **16(1)**, p. 13-31.

14b. Rice, J. E., Rosengren, G. F., *Plan Strain Deformation near a Crack Tip in a Power-Law Hardening Material*, J. Mech. Phys. Solids, 1968,. **16(1)**, p. 1-12.

15. Needleman, A., *A continuum model for void nucleation by inclusion debonding.* J. Appl. Mech., ASME, Trans, 1987. 54(3): p. 525-531.

16. Eshelby, J.D., *The determination of the elastic field of an ellipsoidal inclusion and related problems*, Proceedings of the Royal Society**,** 1957, **A241**, p. 376–396.

17. McDowell, D.L., *Materials design: a useful research focus for inelastic behavior of structural metals.* Theoretical and Applied Fracture Mechanics, 2001. 37(1-3): p. 245-259.

18. Asaro, R. J. and J.R. Rice, *Strain Localization in Ductile Single-Crystals.* Journal of the Mechanics and Physics of Solids, 1977. **25**(5): p. 309-338.

19. Krauss, G., *Steels – Processing, Structure, and Performance.* ASM International, 2005.

20. Hao, S., Moran, B., Liu, W. K., Olson, G. B., *A Hierarchical Multi-Physics Model for Design of High Toughness Steels.* J. Compute-Aided Materials Design, 2003. **10**(2): p. 99-142.

21. Krauss, G., *Microstructure and Performance of Carburized Steel .1. Martensite.* Advanced Materials & Processes, 1995. 147(5): p. 40-46.

22. Hyde, R.S., G. Krauss, and D.K. Matlock, *Phosphorus and Carbon Segregation - Effects on Fatigue and Fracture of Gas-Carburized Modified 4320 Steel.* Metallurgical and Materials Transactions a-Physical Metallurgy and Materials Science, 1994. 25(6): p. 1229-1240.

23. Haasen, P., *Physical Metallurgy*, 1984. Cambridge University Press, Cambridge.

24. Krakauer B. W., Seidman D. N., *Subnanometer scale study of segregation at grain boundaries in an Fe(Si) Alloy*, Acta Mater., 1998, 46(17), p. 6145-6161.

25. Hao, S. and Liu, W. K., *"Moving Particle Finite Element with Global Super-Convergence",* Computer Method in Applied Mechanics and Engineering, 2006, **196**, p. 6059-6072.

26. Rose, J.H., Smith, J.R., and Ferrante, J., *Universal features of bonding in metals.* Physical Review B, 1983. **28**(4): p. 1835-1845.

27. Hao, S., Liu, W. K., and T. Belytschko, *Moving Particle Finite Element Method with Global Smoothness.* Int. J. Numer. Meth. Engr, 2004. **59**: p. 1007-1020.

28. Hao, S., Liu, W. K., Moran, B., Franck Vernerey, F., Olson, G. B., *Multi-Scale Constitutive Model and Computational Framework for the Design of Ultra-High Strength, High Toughness Steels.* Computer Method in Applied Mechanics and Engineering, 2004. **193**(17-20): p. 1865-1908.

29. Tvargaard, V., and Hutchinson, J.W., *The Relation between Crack-Growth Resistance and Fracture Process Parameters in Elastic Plastic Solid.* J. Mech. Phys. Solids, 1992. **40(6)**: p. 1377-1397.

30. S. Hao, H. Park, and W. Liu, *"Moving Particle Finite Element"*, Int. J. Num. Methods Engineering, 2001/2002, **53**(8), p. 1937-1958.

31. Ding, R.G., T.S. Rong, and J.F. Knott, *Phosphorus segregation in 2.25Cr-1Mo steel.* Materials Science and Technology, 2005. 21(1): p. 85-92.

32. Tang, S., A.J. Freeman, and G.B. Olson, *Phosphorus-Induced Relaxation in an Iron Grain-Boundary - a Cluster-Model Study.* Physical Review B, 1993. 47(5): p. 2441-2445.

33. Islam, M.A., et al., *Effect of phosphorus segregation on fracture properties of 2.25Cr-1Mo pressure vessel steel.* Journal of Materials Engineering and Performance, 2003. 12(3): p. 244-248.

34. Alber, I., Bassani, J. L., Khantha, M., Vitek, V., Wang, G. J., *Elastic interfacial waves in discrete and continuous media.* Physical Review B, 1996. 53(13): p. 8398-8410.

35. Asaro, R.J. and A. Needleman, *Flow Localization in Strain-Hardening Crystalline Solids.* Scripta Metallurgica, 1984. **18**(5): p. 429-435.

36. Tvergaard, V. and Hutchinson, J. W., *Effect of Strain Dependent Cohesive Zone Model on Predictions of Interface Crack Growth*, Int. J. Solid and Structs, 1996. **33**(20-22): p. 3297-3308.

37. Quigley, C. and Parks, D. M., "The Finite Deformation Field surrounding a Mode I Plane Strain Crack in a Hyperelastic Incompressible Material under Small-Scale Nonlinearity", Int. J. Fracture, 1994, **65**, p. 75-96.

38. Xu, X. P. and Needleman, A., *Numerical Simulations of Fast Crack Growth in Brittle Solids*, J. Mech. Phys. Solid, 1994. **42**(9): p. 1397-1413.

39. Fracture: A Topical Encyclopaedia of Current Knowledge, Vol.2, edts. Liebowitz, H., Academic Press, New York, 1970.

40. Begley, J. A., Landes, J. D., The *J-integral as a fracture criterion, fracture toughness*, ASTM, STP514, 1972, p.1-20.

41. Hutchinson, J. W., Paris, P. C., *Stability analysis of J-controlled crack growth*, Elastic-Plastic Fracture, ASTM STP668, edit. J. D. Landes and Bergley, 1979, p.26-67.

42. Bazant, Z.P., *Scaling laws in mechanics of failure*, ASCE Journal of Engineering Mechanics **119**, p.1828– 1844.

43. Hsia, K. J., Argon, A. S., Parks, D. M., *Effects of grain-boundary sliding on creep-constrained boundary cavitation and creep deformation*, Mechanics of Materials, 1991,. **11(1)**, p. 43-62. and 1993, **14**(4), p. 313-314

44. NRL, *DoD Plane Wave: A General Scalable Density Functional Code*. 2002.

45. WIEN2k, *An Augmented Plane Wave Plus Local Orbitals Program for Calculating Crystal Properties*, 2000.

46. Krakauer, H. and A.J. Freeman, *Linearized Augmented Plane-Wave Method for the Electronic Band-Structure of Thin-Films.* Physical Review B, 1979. **19**(4): p. 1706-1719.

47. Mehl, M.J. and D.A. Papaconstantopoulos, *Applications of a tight-binding total-energy method for transition and noble metals: Elastic constants, vacancies, and surfaces of monatomic metals.* Physical Review B, 1996. **54**(7): p. 4519-4530.

48. Daw, M.S. and M.I. Baskes, *Embedded-Atom Method - Derivation and Application to Impurities, Surfaces, and Other Defects in Metals.* Physical Review B, 1984. **29**(12): p. 6443-6453.

49 Baskes, M.I., *Embedded Atom Method Atomistic Calculations of the Dynamic Interaction of an Edge Dislocation in Nickel with Helium Clusters.* Journal of Metals, 1988. **40**(11): p. 123-123.

50. Zienkiewicz, O.C., *The Finite Element in Engineering Science,*. 1972: McGraw Hill.

51. Oden, J.T., *Finite Elements of Nonlinear Continua*. 1972, New York: McGraw-Hill Book Company.

52. Hughes, T.J.R., *The Finite Element Method*. 1987, New Jersey: Prentice-Hall.

53. Belytschko, T., Liu, W.K., and Moran, B., *Nonlinear Finite Elements for Continua and Structures*. 2000, New York: John Wiley & Sons.

54. Weertman J. and Weertman, J. R., Elementary Dislocation Theory 1964, New York: Macmillan. Pub.

55. Abdel-Tawab K, Rodin G. J., *Fracture size effects and polycrystalline inhomogeneity*, ASCE Journal of Engineering Mechanics, 2004, **119**, p.1828–1844.

56. Birch, F., *The Effect of Pressure upon the Elastic Parameters of Isotropic Solid*. J. Appl. Phys., 1938, **9**, p.279-288.

57. Choly, N., Lu, G., Weinan, E., Kaxiras, E., *Multiscale Simulations in Simple Metals: A Density-Functional-Based Methodology*. Phys. Review, B, 2005, **71**, 094101, p. 1-16.

58. Diestler, D. J., *Coarse-Grained Description of Multiple Scale Processes in Solid System*. Phys. Review, B, 2002, **66**, 184104, p.1-7.

59. Marcos, J. Manosa, L., Planes, A., Casanova, F., Batlle, X., Labarta, A., *Multiscale Origin of the Magnetocaloric Effect in Ni-Mn-Ga Shape-Memory Alloys*. Phys. Review, B, 2003, **68**, 094401, p.1-7.

60. Tadmor, E. B., Philips, R., Ortiz, M., *Mixed Atomistic and Continuum Models of Deformation in Solids*. Langmuir, 1996, **12(19)**, p.4529-4534.

61. Tadmor, E. B., Philips, R., Ortiz, M., *Quasicontinuum Analysis of Defects in Solids*. Philos. Mage. A., 1996, **73 (6)**, p.1529-1563.

62. Liu, W. K., Hao, S., Belytschko, T., Li, S., Chang, C. T., *Multi-Scale Methods*. Int. J. Num. Methods Engineering, 2000, **47**, p. 1343-1358.

63. Ostoja-Starzewski, M., *Bounding of Effective Thermal Conductivities of Multiscale Materials by Essential and Natural Bundary Conditions*. Phys. Review, B, 1996, **54**(1), p.278-285.

64. Bishop, J.F., and Hill, R., *A theory of the plastic distortion of polycrystalline aggregate under combined stresses.* Phil. Mag, 1951. **42**: p. 414-427.

65. Hao, S., Olson, G. B., *Multi-Scale Mechanical Optimization for Design of High Strength, High Toughness Austenite-Martensite Alloys (manuscript in preparing)* in *The 5th International Conference on Martensite Transformation (ICOMAT05).* 2005: Shang Hai, China.

66. Arsenlis, A., Parks, D. M., *Modeling the Evolution of Crystallographic Dislocation Density in Crystal Plasticity*. J. Mech. Phys. Solid, 2002, **50(9)**, p. 1979-2009.

67. Ashcroft, N.W., Mermin, N. D., *Solid State Physics*. 1976, Fort Worth: Saunders College Publishing.

68. Fleck, N.A., and Hutchinson, J.W., *Strain gradient plasticity.* Advances in Applied Mechanics, 1997. **33**: p. 295-361.

69. Gao, H.J., Huang, Y., Nix, W.D., and Hutchinson, J.W., *Mechanism-Based Strain Gradient Plasticity - I. Theory.* Journal of Mechanics and Physics of Solids, 1999. **47**: p. 1239-1263.

70. Singh, D. J., *Planewaves, Pseudopotentials and the LAPW Method.* Kkywer Academic Pub., 1994.

71. Wimmer, E., Krakauer, H., Weinert, M., Freeman, A. J., *Full-Potential Self-Consistent Linearized-Augmented-Plane-Wave Method for Calculating the Electronic-Structure of Molecules and Surfaces - O2 Molecule.* Physical Review B, 1981. **24**(2): p. 864-875.